JOURNAL OF MAGNETIC RESONANCE IMAGING 34:420–428 (2011)

Original Research

Model-Based Nonlinear Inverse Reconstruction for T2 Mapping Using Highly Undersampled Spin-Echo MRI

Tilman J. Sumpf, Dipl-Ing,* Martin Uecker, PhD, Susann Boretius, PhD, and Jens Frahm, PhD

Purpose: To develop a model-based reconstruction technique for T2 mapping based on multi-echo spin-echo MRI sequences with highly undersampled Cartesian data encoding.

Materials and Methods: The proposed technique relies on a nonlinear inverse reconstruction algorithm which directly estimates a T2 and spin-density map from a train of undersampled spin echoes. The method is applicable to acquisitions with single receiver coils but benefits from multi-element coil arrays. The algorithm is validated for trains of 16 spin echoes with a spacing of 10 to 12 ms using numerical simulations as well as human brain MRI at 3 Tesla (T).

Results: When compared with a standard T2 fitting procedure using fully sampled T2-weighted images, and depending on the available signal-to-noise ratio and number of coil elements, model-based nonlinear inverse reconstructions for both simulated and in vivo MRI data yield accurate T2 estimates for undersampling factors of 5 to 10.

Conclusion: This work describes a promising strategy for T2-weighted MRI that simultaneously offers accurate T2 relaxation times and properly T2-weighted images at arbitrary echo times. For a standard spin-echo MRI sequence with Cartesian encoding, the method allows for a much higher degree of undersampling than obtainable by conventional parallel imaging.

Key Words: quantitative MRI; T2 mapping; T2 relaxivity; human brain; model-based reconstruction; nonlinear inversion
J. Magn. Reson. Imaging 2011;34:420–428.

QUANTITATIVE EVALUATIONS OF MRI parameters are of utmost importance for both diagnostic imaging of patients and biomedical research involving experimental animals. In this respect, the T2 relaxation time (or relaxation rate 1/T2) of tissue water protons is of particular relevance as it reveals pronounced sensitivity to pathologic tissue alterations. The current method of choice for measuring T2-weighted images is the fast spin-echo MRI sequence originally proposed as single-shot RARE (1). To speed up the acquisition process, the train of successively refocused spin echoes is differently phase encoded which allows for a corresponding reduction of the number of echo trains or excitations. Unfortunately, however, a composite *k*-space of Fourier lines with different echo times leads to T2-weighted images with a mixed contrast (also depending on the ordering of lines in *k*-space) and further causes a certain degree of spatial blurring and ringing due to the associated alteration of the point-spread function.

A more flexible and quantitative image analysis may be achieved by estimating parameter maps of T2 and spin density from fully sampled *k*-space datasets acquired at different echo times. The approach enables retrospective calculations of T2-weighted "synthetic" images at arbitrary TE values and provides access to quantitative relaxation rates—though at the expense of long scan times. Several methods have been proposed to overcome this limitation. For example, in parallel imaging the complementary spatial information of the sensitivity profiles from multiple receiver coils is exploited to reduce the number of phase-encoding steps (2,3). Alternatively, methods based on compressed sensing can be applied to MRI, if the images may be considered as sparse in suitably chosen domains (4). Most recently, such sparsity transforms were extended to the T1 and T2 parameter space and used for model-based reconstructions of corresponding maps (5). Specifically with respect to T2 mapping, it has also been proposed to iteratively fit the parameters of a mono-exponential decay to undersampled radial *k*-space data with the use of a Projection onto Convex Sets (POCS) algorithm (6) or to jointly estimate a spin-density and T2 map as the solution of a nonlinear inverse problem (7). In the latter case, undersampled spin-echo MRI acquisitions used radial *k*-space trajectories and multiple receiver coils (i.e. parallel imaging). A related idea has been applied

Biomedizinische NMR Forschungs GmbH am Max-Planck-Institut für biophysikalische Chemie, Göttingen, Germany.

*Address reprint requests to: T.J.S., Biomedizinische NMR Forschungs GmbH am Max-Planck-Institut für biophysikalische Chemie, 37070 Göttingen, Germany. E-mail: tsumpf@gwdg.de

Received August 13, 2010; Accepted April 6, 2011.

DOI 10.1002/jmri.22634
View this article online at wileyonlinelibrary.com.

to simultaneously reconstruct dynamic T2* and field maps in functional MRI (8).

In this article, we expand the general concept outlined in (7) and evaluate its performance for reconstructions from undersampled Cartesian data encodings because Cartesian phase encoding is still most widely used in clinical practice and less sensitive to gradient imperfections. We introduce an automatic gradient-scaling method to avoid ill-conditioning of the inverse reconstruction problem and demonstrate a dedicated undersampling pattern which minimizes aliasing artifacts in the parameter maps. Although the use of multiple receiver coils further improves the quality of the reconstruction, the method allows for a pronounced degree of undersampling even without parallel imaging. This is because—in a formal sense—complementary spatial encodings may not only be distributed among different coils, but also among different echo times. The accuracy of the approach is determined for simulated data and experimentally validated for T2 mapping of the human brain.

MATERIALS AND METHODS

Model-Based Nonlinear Inverse Reconstruction

The MRI signal obtained from a single receiver coil with uniform sensitivity is given by

$$s(t) = \int M(\vec{r}) \cdot e^{-i\vec{r}\vec{k}(t)} d\vec{r}, \qquad [1]$$

where $M(\vec{r})$ denotes the transverse magnetization, $\vec{r}$ is a position in image space and $\vec{k}(t)$ the chosen *k*-space trajectory. For spin-echo experiments, the magnetization at echo time TE can be modeled by an exponential decay

$$M_{TE}(\rho, R) = \rho(\vec{r}) \cdot e^{-R(\vec{r})\cdot TE} \qquad [2]$$

with $\rho(\vec{r})$ the spin density and $R(\vec{r}) = 1/T_2(\vec{r})$ the tissue-specific transverse relaxation rate (neglecting the T2 decay during the acquisition window).

In conventional settings, ρ and *R* are calculated on a pixel-by-pixel basis in image space by curve fitting of images that are obtained for different echo times by inverse discrete Fourier transform (DFT). However, if the number of samples per echo time is reduced such that the *k*-space trajectory violates the Nyquist criterion, a direct application of the inverse DFT leads to aliasing in the images and hence to incorrect results.

To overcome this problem, it has been proposed to include the forward DFT in the signal model to synthesize fully sampled *k*-space data from estimated maps, and then use a cost function

$$\Phi(x) = \frac{1}{2}\sum_{TE} ||P\ DFT\ M_{TE}(x) - s_{TE}||_2^2 \qquad x = \begin{pmatrix} \rho \\ R \end{pmatrix} \qquad [3]$$

to quantify the conformity of the synthesized data with the sampled data (7). The projection of the synthesized data on the measured trajectory is performed by the operator *P* which, for the Cartesian case, represents a multiplication with a binary sampling mask. While P and DFT are linear operators, the model M represents a nonlinear operator. Therefore, a nonlinear numerical optimization algorithm was used to minimize the cost function

$$\hat{x} = \arg\min\{\Phi(x)\} \qquad [4]$$

and to find a common solution $\hat{x}$ for all acquired *k*-space positions and echo times. In fact, this model-based reconstruction condenses the total information into only two distinct parameter maps, and thereby highlights the pronounced redundancy in the original data which in turn may be exploited to reduce the number of phase-encoding steps per echo.

Model Limitations and Undersampling Scheme

If Eq. [2] would correctly model the relaxation process for every pixel, artifact-free reconstructions should be achievable with arbitrary sampling patterns that collect sufficient independent data to cope with the existing unknowns. However, the signal in real images does not always comply with the assumption of a mono-exponential T2 decay. Besides random errors due to noise, systematic model violations may originate from sequence imperfections, partial volume effects and truncation artifacts (Gibbs ringing). The latter problem arises at discontinuities in image space, which cannot accurately be recovered from a limited number of discrete Fourier coefficients (9–12). Thus, the minimum of the cost function [3] will be greater than zero even for fully sampled and noiseless data, while reconstructions of parameter maps from undersampled data may be affected by aliasing artifacts.

The practical impact of possible aliasing artifacts strongly depends on the sampling pattern. For example, estimated parameter maps that rely on a periodically interleaved Cartesian undersampling pattern (schematically depicted in Fig. 1, left) often comprise aliased copies of image regions that violate the underlying model assumptions. The coherence of these artifacts can be reduced with the use of a random pattern as chosen for reconstructions based on compressed sensing (4). Because the randomization of *k*-space acquisitions works most efficiently when applied in two dimensions, this strategy is most promising for 3D MRI. For the present case of 2D spin-echo MRI, we achieved better results by the application of a blocked pattern (Fig. 1, center and right), which is similar to the acquisition scheme used for linearly phase-encoded fast spin-echo MRI.

Multiple Receiver Coils

If multiple receiver coils are available, the reconstruction can be combined with parallel imaging strategies by including the sensitivity profiles C_c of the coil elements *c* into the signal model. Accordingly, Eq. [3] is extended to

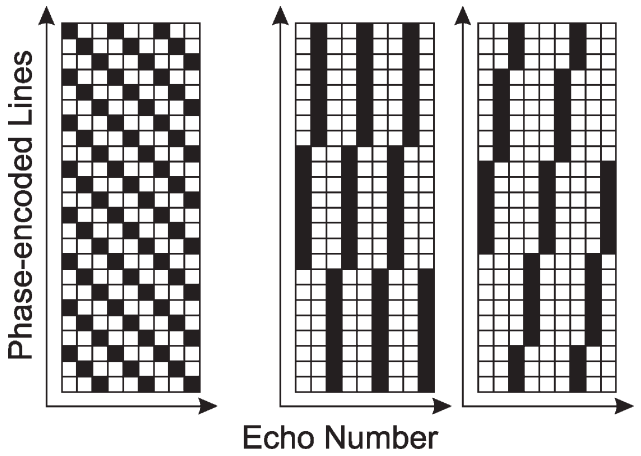

Figure 1. Cartesian encoding with (left) a three-fold accelerated interleaved sampling scheme (middle) a blocked undersampling scheme with acceleration factor 3 and (right) 4. The example refers to a *k*-space of 24 phase-encoded lines and 9 echoes. Solid symbols represent acquired lines, while lines not measured are represented by open symbols.

$$\Phi(x) = \frac{1}{2}\sum_c \sum_{TE} ||P\ DFT\ (M_{TE}(x)C_c) - s_{TE,c}||_2^2. \quad [5]$$

This can improve the condition number of the equation system, but requires estimates of the coil sensitivities C_c. For a blocked undersampling scheme the centrally arranged *k*-space samples of the first echo can be used to create such coil profiles from a low-resolution reference image. Even better coil profiles may be obtained using a nonlinear inverse algorithm previously developed for parallel imaging (13). Here this algorithm was constrained such as to shift all phase information into the complex coil sensitivities and applied to a fully sampled *k*-space obtained by the combination of data from multiple echoes. The resulting sensitivities were kept constant during the minimization of the cost function [5], while the parameter maps ρ and R were assumed to be real.

Optimization and Gradient Scaling

For the minimization of the nonlinear cost function we used the CG-Descent algorithm (14). Because its success and speed depend on the relative scaling of the partial derivatives of the cost function with respect to the components in x, a heuristically chosen scaling factor for the echo-time vector was proposed in (7). Here, we introduce a data-driven method to automatically determine proper scaling factors.

For equally spaced echo times TE_n, the signal model in [2] can be simplified to:

$$M_n(\rho, \hat{R}) = \rho \cdot \hat{R}^n, \quad [6]$$

with $\hat{R} = \exp(-R \cdot TE_1)$ and n being the echo number. By introducing the two additional scaling variables L_ρ and L_R the modified model function reads:

$$M_n(\tilde{\rho}, \tilde{R}) = L_\rho \tilde{\rho} \cdot (L_R \tilde{R})^n. \quad [7]$$

Assuming $\tilde{\rho}, \tilde{R}$ and P to be real, the gradient of the cost function is

$$\begin{aligned}
\nabla\Phi(\tilde{x}) &= \begin{pmatrix} \frac{d\phi}{d\tilde{\rho}} \\ \frac{d\phi}{d\tilde{R}} \end{pmatrix}, \\
\frac{d\phi}{d\tilde{\rho}} &= \sum_c \sum_n L_p (L_R \tilde{R})^n K_{c,n} \\
&= \sum_c \sum_n L_p\ \hat{R}^n\ K_{c,n}, \\
\frac{d\phi}{d\tilde{R}} &= \sum_c \sum_n n\ L_R^n \tilde{R}^{n-1}\ L_\rho \tilde{\rho}\ K_{c,n} \\
&= \sum_c \sum_n n\ L_R\ \hat{R}^{n-1}\ \rho\ K_{c,n} \\
\text{with}\ \ K_{n,c} &= \bar{C}_c DFT^{-1}(P\ DFT\ M_n(\tilde{x})C_c - s_n).
\end{aligned} \quad [8]$$

where $\bar{C}_c$ refers to the complex conjugate coil sensitivities. As a result, the two main components of the gradient near an estimated solution can be equalized using the diagonal scaling matrices

$$\begin{aligned}
L_\rho &= \left(\sum_n \hat{R}^n\right)^{-1}, \\
L_R &= \left(\sum_n n\ \hat{R}^{n-1}\ \rho\right)^{-1}.
\end{aligned} \quad [9]$$

With the blocked undersampling scheme, a low-resolution approximation of $\hat{R}$ and ρ may be calculated before the main reconstruction by using the central *k*-space samples available at different echo times. However, a direct calculation of the scaling matrices from such estimates can provoke disadvantageous gradient amplifications within noisy or low-intensity image regions. A robust solution was obtained by reducing the diagonal scaling matrices to scalar values derived from the respective means of the low-resolution parameter maps.

Implementation

We used a C implementation of the CG-Descent algorithm (14), while the routines for the cost function were written in MATLAB (MathWorks, Natick, MA). The number of CG iterations was set to a fixed number of 200 for all reconstructions in this study. The computations took approximately 70 s for a dataset with 16 echoes and a 192 × 192 image matrix on a single core of a standard desktop PC equipped with an Intel Core2 Duo CPU (2.66 GHz). This time proportionally increased with the number of echoes and coil elements.

Simulations

To validate the accuracy of the approach for a single receiver coil, we used simulated data for two numerical phantoms with multiple objects exhibiting equal spin density but different T2 relaxation times ranging from 50 to 1000 ms. Simulated *k*-space samples were derived from superimposed circles using the

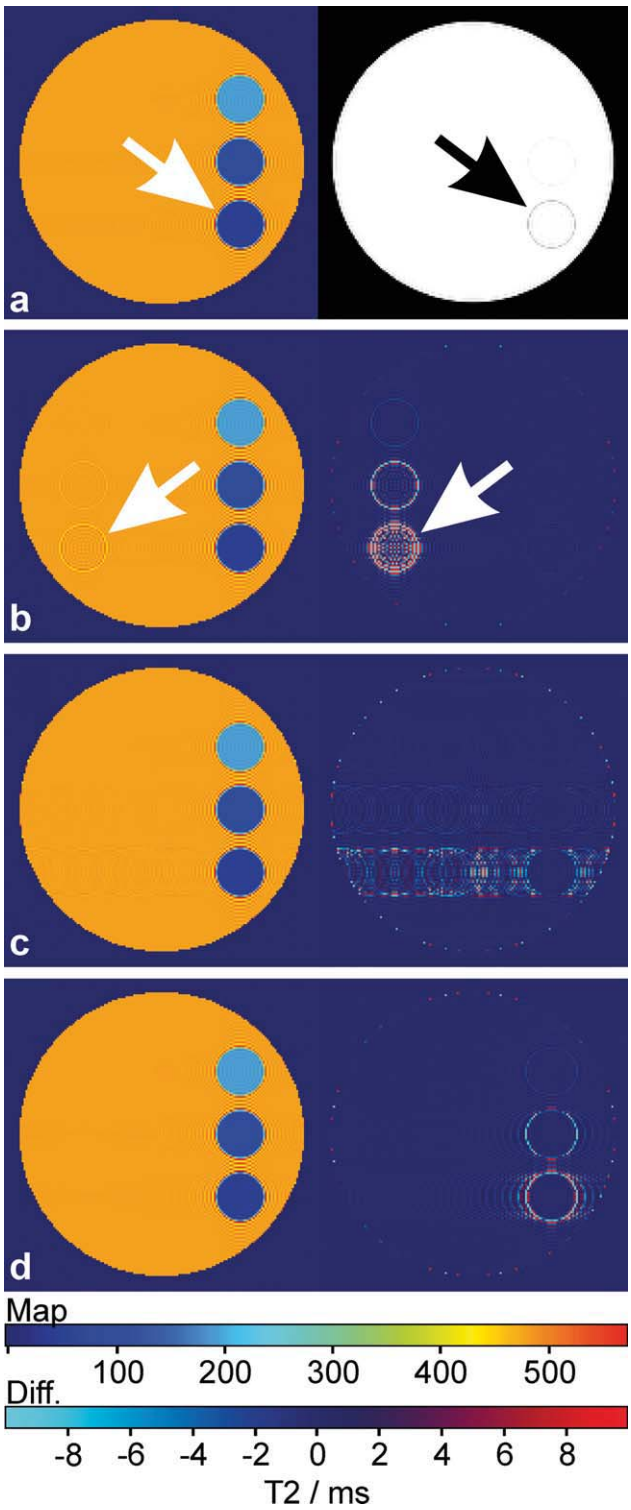

Figure 2. (Left) Estimated T2 maps of a noiseless numerical phantom from (**a**) fully sampled data as well as undersampled data using an interleaved (**b**), a random (**c**), and a blocked scheme (**d**) (16 echoes, $\Delta TE = 10.0$ ms, undersampling factor 2, single receiver coil). (Right) The maps represent the corresponding spin-density map (a) and T2 difference maps with respect to the fully sampled reconstruction (b–d). Residual artifacts (arrows) refer to ringing in (a) and aliasing in (b), the latter of which is reduced in (c) and (d). The T2 relaxation times of the compartments are 50 ms (bottom), 100 ms (middle), 200 ms (top), and 500 ms (surrounding).

analytical Fourier space representation of an ellipse, i.e., a first-order Bessel function of the first kind. The simulated data comprised 16 echoes with an echo spacing of $\Delta TE = 10$ ms and a matrix size of 160×160. The presence of noise was simulated by adding Gaussian noise with a standard deviation (SD) ranging from 1% to 5% of the uniform spin-density signal. For a given experimental condition and echo train, this was accomplished by adding uncorrelated noise (same amplitude) to the real and imaginary parts of the *k*-space data of all echoes. During the analysis, a noise mask was applied to all parameter maps to eliminate regions with values below 15% of the arithmetic mean of ρ. Low R values were limited to a minimum of 0.2 s^{-1} corresponding to a maximum T2 value of 5000 ms.

Human Studies

A young healthy adult with no known abnormality participated in this study and gave written informed consent before each MRI examination at 3T (Tim Trio, Siemens Healthcare, Erlangen, Germany). While radiofrequency excitation was accomplished with the use of a body coil, signal reception was performed either by a single quadrature head coil or a 32-element head coil. For this proof-of-principle study, only five sections with a resolution of $1.0 \times 1.0 \times 4.0$ mm^3 were acquired using a commercial spin-echo MRI sequence with an echo spacing of $\Delta TE = 12.2$ ms. The original dataset involved 32 echoes with full *k*-space sampling. However, because the latest echoes exhibited very low SNR and because the signal strength of the first echo was systematically too low and the sequence not correctable by simple means, the analyzed data were restricted to echoes 2 to 17. Different undersampling factors (blocked scheme) were realized by selecting respective *k*-space lines from the fully sampled data. For a matrix size of 192×160 and a repetition time of TR = 3000 ms the acquisition time without undersampling was 8 min.

RESULTS

Undersampling Scheme

Figure 2a shows a T2 and spin-density map reconstructed from fully sampled *k*-space data without noise for a numerical phantom and a single receiver coil. The circular shape of the compartments deliberately involves partial volume effects with the surrounding, so that affected voxels exhibit a multi-exponential signal behavior. In addition, the estimated maps reveal residual ringing artifacts at T2 discontinuities which are most pronounced for the strongest T2 difference (white arrow) between the first compartment (50 ms) and its surrounding (500 ms). As a consequence, both the compartment borders and the adjacent ringing reappear in the reconstructed spin-density map (black arrow).

The application of an interleaved undersampling pattern is demonstrated in Figure 2b. Despite the fact that the undersampling factor was only 2, aliased

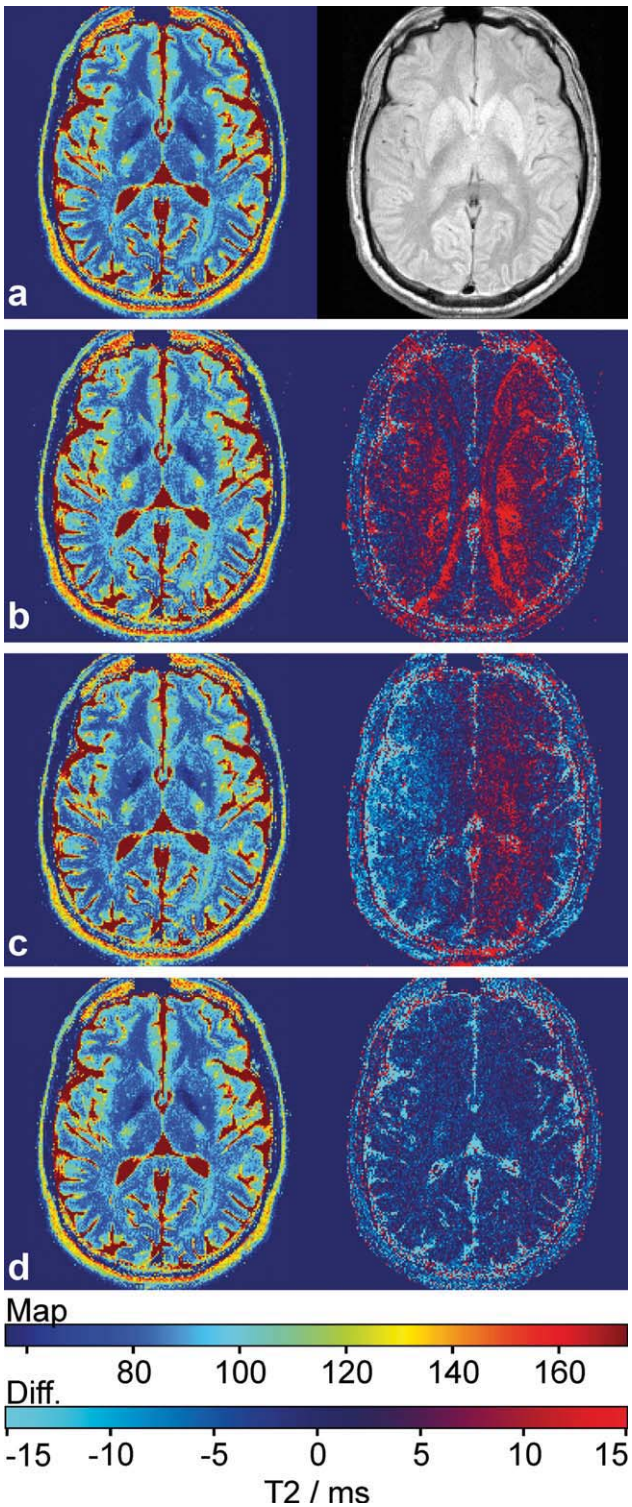

Figure 3. (Left) Estimated T2 maps of the human brain from fully sampled data as well as undersampled data (**a**) using an interleaved (**b**), a random (**c**), and a blocked scheme (**d**) (16 echoes, ΔTE = 12.2 ms, undersampling factor 2, single receiver coil). (Right) The maps represent the corresponding spin-density map (a) and T2 difference maps with respect to the fully sampled reconstruction (b–d) (parameters as in Fig. 2).

copies of the object's discontinuities become visible in the reconstructed maps (arrows). The situation is improved when using a random pattern as shown in Figure 2c. Similar to Figure 1 (left) the applied pattern was designed in an interleaved manner, where samples from odd echoes were selected randomly while even echoes fill the previously open *k*-space positions. This strategy turned out to be more efficient than an echo-independent random sampling. As can be seen in the difference maps, the aliasing artifacts are weaker and spread out along the phase-encoding direction of the image. Finally, Figure 2d demonstrates that an even better suppression of artifacts was achieved by a blocked undersampling scheme despite residual artifacts restricted to T2 discontinuities and respective structural borders.

A similar comparison of different sampling strategies for MRI of the human brain is summarized in Figure 3. The results are in agreement with and confirm the observations made for simulated data. Based on these findings, all applications of the model-based reconstruction to human MRI data were accomplished with the use of a blocked undersampling scheme.

Quantitative Accuracy

The left column in Figure 4 shows the reconstructed T2 maps of a noiseless numerical phantom for different undersampling factors using a blocked undersampling scheme and a single receiver coil. The

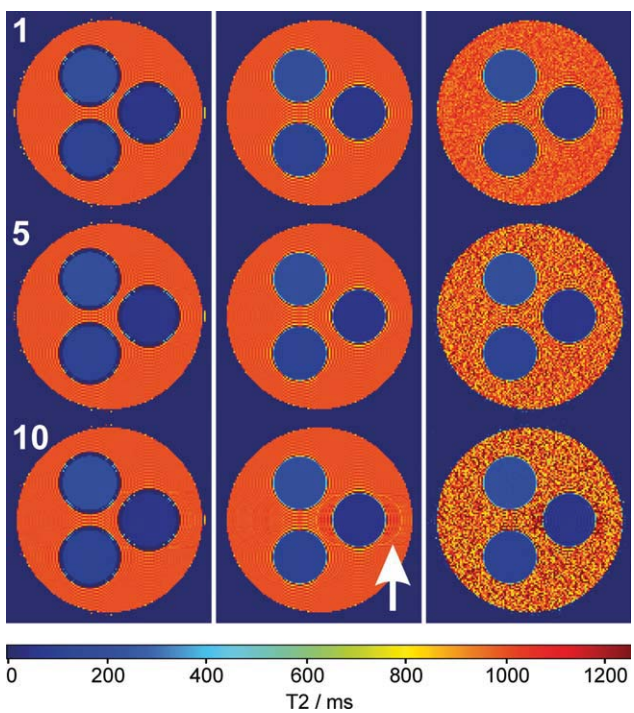

Figure 4. Model-based reconstructions of T2 maps from numerical phantoms for undersampling factors of 1, 5, and 10 (16 echoes, ΔTE = 10.0 ms, blocked scheme, single receiver coil). (Left) No noise, T2 compartments isolated from the surrounding, (middle) no noise, T2 compartments directly embedded in the surrounding, (right) same as (middle) but with noise corresponding to 1% SD of the initial spin-density signal for all echoes. The T2 relaxation times of the compartments are 50 ms (right), 100 ms (lower left), 200 ms (upper left), and 1000 ms (surrounding).

Table 1
T2 Relaxation Times From Model-Based Reconstructions of a Numerical Phantom*

Undersampling	T2 = 50 ms	T2 = 100 ms	T2 = 200 ms	T2 = 1000 ms
No noise, isolated compartments				
Standard fitting	50.0 ± 2.2	100.0 ± 1.9	200.0 ± 2.5	1000.0 ± 6.6
1	50.0 ± 2.3	100.0 ± 1.9	200.1 ± 2.4	1000.3 ± 6.6
5	50.0 ± 2.6	100.0 ± 2.0	200.0 ± 2.5	999.6 ± 7.4
8	50.0 ± 3.5	100.0 ± 2.2	200.1 ± 2.7	999.3 ± 6.2
10	50.3 ± 5.9	100.0 ± 2.7	200.0 ± 2.8	1000.0 ± 6.8
No noise, compartments without isolation				
Standard fitting	50.1 ± 2.6	100.0 ± 2.5	200.0 ± 3.0	1000.0 ± 6.6
1	50.0 ± 2.6	100.0 ± 2.5	200.0 ± 3.0	999.9 ± 6.6
5	50.1 ± 3.1	100.0 ± 2.6	200.0 ± 3.1	1000.0 ± 5.4
8	50.2 ± 4.2	100.1 ± 2.9	200.1 ± 3.2	1000.0 ± 10.2
10	50.6 ± 6.5	100.1 ± 3.5	200.0 ± 3.3	1000.4 ± 9.3
Noise level = 1% (compartments without isolation)				
Standard fitting	50.1 ± 2.7	100.1 ± 2.7	200.1 ± 4.4	1004.8 ± 57.8
1	50.0 ± 2.7	100.0 ± 2.6	200.1 ± 4.5	1005.3 ± 58.1
5	50.1 ± 3.9	99.9 ± 4.0	200.5 ± 9.4	1021.9 ± 152
8	50.7 ± 7.1	100.2 ± 5.7	200.6 ± 10.7	1039.2 ± 208
10	52.9 ± 12.9	100.8 ± 6.6	201.1 ± 12.0	1058.5 ± 260
Noise level = 5% (compartments without isolation)				
Standard fitting	52.8 ± 4.6	102.3 ± 7.3	201.8 ± 17.3	1137.0 ± 484
1	50.1 ± 4.4	101.2 ± 7.6	200.3 ± 16.5	1138.7 ± 521
5	51.5 ± 14.1	104.3 ± 18.3	208.0 ± 44.6	n.a.
8	55.2 ± 22.7	107.0 ± 31.3	217.6 ± 65.2	n.a.
10	54.1 ± 28.1	110.0 ± 37.3	255.8 ± 498	n.a.

*T2 values (ms) represent mean ± SD (16 echoes, ΔTE = 10 ms, single receiver coil), n.a. = not available. Noise levels (for all echoes) are characterized by their SD in percent of the uniform spin-density signal. Standard nonlinear least-squares fitting refers to a set of fully sampled T2-weighted magnitude images.

compartments of this phantom have been encircled by distinct borders of void signal intensity, precluding partial volume effects with the surrounding. The remaining source of signal deviations from a strictly mono-exponential decay is, therefore, reduced to truncation artifacts. In addition to ringing, the reconstructed parameter maps remain free of visible artifacts up to an undersampling factor of 9. The result for an undersampling factor of 10 slightly differs from the fully sampled map by a barely visible residual aliasing artifact around the compartment with the highest relaxivity difference to the surrounding.

The influence of partial volume effects on the reconstruction is demonstrated in the middle column of Figure 4, where the signal void between the compartments has been removed. The aliasing effect for an undersampling factor of 10 is now more pronounced (arrow). In the presence of Gaussian noise with a SD that corresponds to 1% of the spin-density signal, all aliasing artifacts become invisible as shown in the right column of Figure 4.

A quantitative ROI-based analysis of mean T2 estimates is summarized in Table 1. As a "gold standard," all values are compared with the results of a nonlinear least-squares fit of a set of T2-weighted magnitude images that were obtained by Fourier transformation of the respective fully-sampled *k*-space data. The influence of Gaussian noise has been evaluated for SD levels of 1% and 5%, which correspond to SNR values of 100 and 20 (single coil). For comparison, the fully sampled studies of the human brain resulted in a SNR above 200 (initial echoes) for multi-channel recordings, and above 40 for the single coil. Simulations were performed for undersampling factors of 1, 2, 5, and 10. For noiseless data, all T2 estimates closely agree with the values obtained by standard fitting and are very accurate up to the highest undersampling factor of 10. Residual T2 deviations have to be ascribed to truncation artifacts, as the removal of the compartment isolations only causes negligible changes in the SD values, and the reconstruction accuracy for ringing-free phantoms reaches the machine precision for all undersampling factors up to 15 (not shown).

Similar good results are obtained for the condition with 1% noise, although at the expense of slightly increased SD values for the T2 estimates. In this case, the mean T2 values up to 200 ms deviate from the correct values by less than 2% for undersampling factors up to 8. Larger errors of up to 4% for the compartment with T2 = 1000 ms must be ascribed to the fact that the 16 simulated echoes covered a period of only 160 ms which is far from being adequate for long T2 relaxation times. This effect becomes stronger for higher acceleration factors and noise levels. While the results for a 5% noise level still allow for an undersampling factor of 5, when accepting a 4% error for T2 estimates up to 200 ms, some T2 estimates in the surrounding become limited by the applied mask. Pertinent results are discarded.

Human Studies

Figure 5 shows spin-density and T2 maps of the human brain which are reconstructed with different degrees of undersampling using the blocked scheme

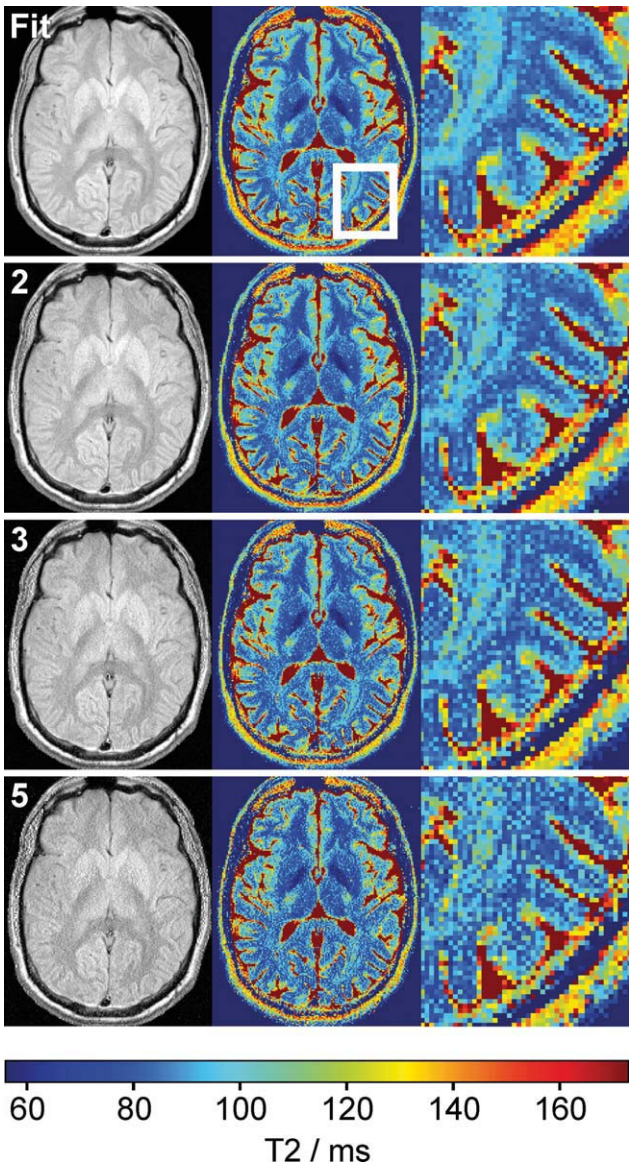

Figure 5. Standard fitting (fully sampled *k*-space data) versus model-based reconstructions of (left) spin-density and (middle, right) T2 maps of the human brain for a single receiver coil and undersampling factors of 2, 3, and 5 (16 echoes, ΔTE = 12.2 ms, blocked scheme).

and a single-element head coil for data acquisition. Again, they are compared with a nonlinear least-squares fit of fully sampled magnitude images. The resulting parameter maps from the model-based nonlinear inverse reconstruction remain free of visible artifacts up to an undersampling factor of 5. However, with this coil the SNR decrease for fewer acquisitions becomes already visible for undersampling factors larger than 2. The experiment was, therefore, repeated with a 32-element head coil as shown in Figure 6. In this case, the magnitude images for the least-squares fit were obtained from the sum-of-squares of the Fourier transformed data of all individual coil elements. The nonlinear inverse reconstruction benefits from the much better SNR and yields acceptable T2 maps for an undersampling factor of at least 5. The reconstructions for a factor of 10 exhibit small artifacts such as vertical ghosts near the hemispheric fissure.

Complementing the determination of parameter maps, model-based reconstructions allow for the estimation of T2-weighted images at arbitrary echo times. Figure 7 depicts respective images (same section as in Fig. 6) for an undersampling factor of 5 and echo times that range from spin-density contrast to weak, moderate, and strong T2 contrast. In contrast to conventional fast spin-echo images, these images exhibit "true" T2 contrast for the chosen echo time (rather than a mixed contrast of several echo times) and also remain free from blurring which arises from a modulation of the point-spread function when combining phase-encoded echoes with different intensities.

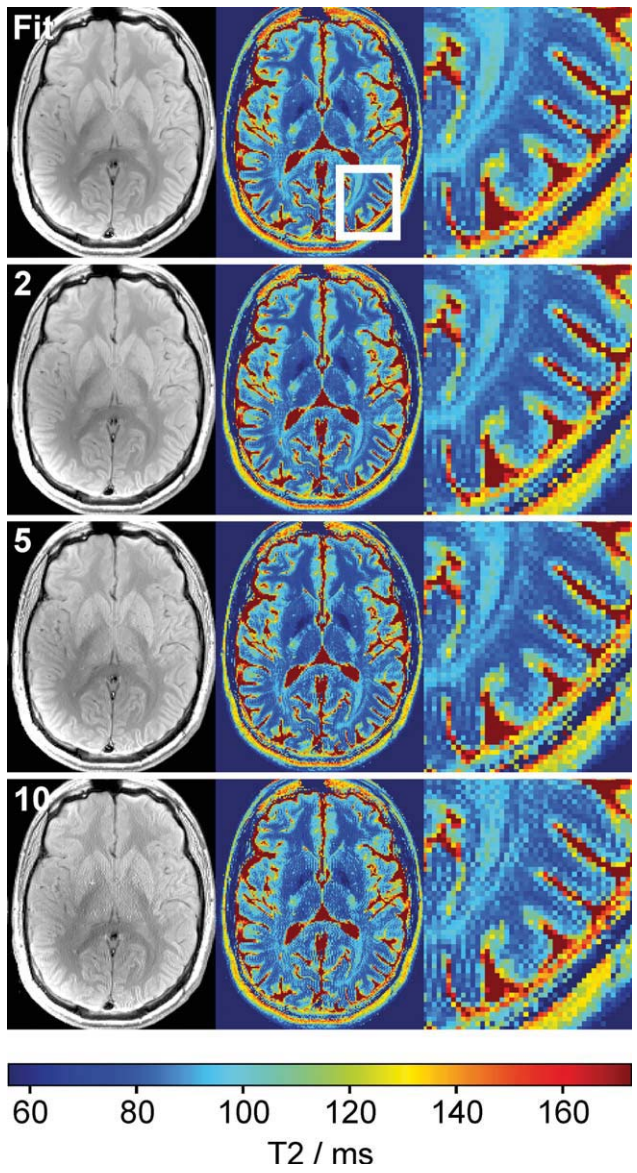

Figure 6. Standard fitting (fully sampled *k*-space data) versus model-based reconstructions of (left) spin-density and (middle, right) T2 maps of the human brain for a 32-element coil and undersampling factors of 2, 5, and 10 (16 echoes, ΔTE = 12.2 ms, blocked scheme).

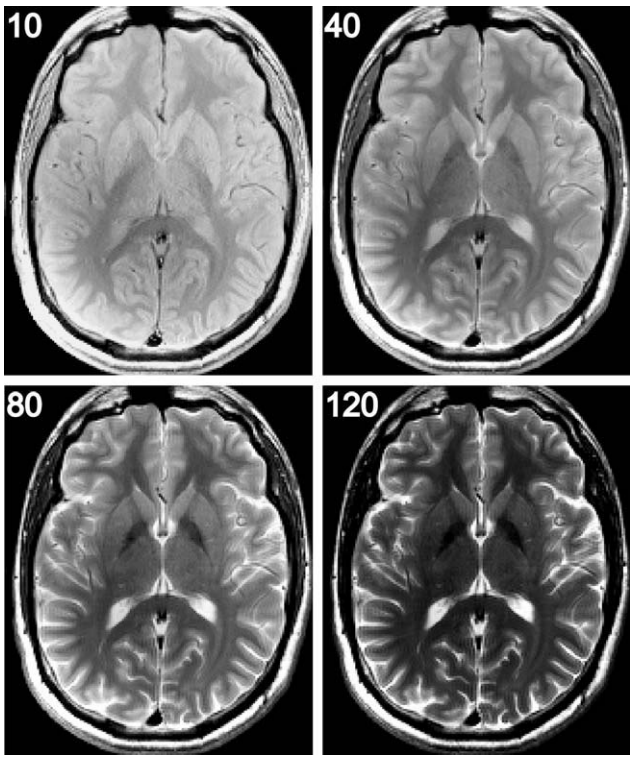

Figure 7. "Synthetic" T2-weighted images from model-based reconstructions of a spin-density and T2 map of the human brain with an undersampling factor of 5 (same section and parameters as in Fig. 5). The echo times TE = 10, 40, 80, and 120 ms correspond to spin-density contrast as well as weak, moderate, and strong T2 contrast, respectively.

Table 2 summarizes T2 estimates for different regions-of-interest in the human brain as a function of the degree of undersampling. The T2 values obtained from the model-based reconstruction reveal a surprisingly good agreement with those obtained from the fully sampled datasets even for undersampling factors up to 10. For the fully sampled data, the T2 values of the least-squares fit are slightly higher than those obtained by model-based reconstruction. This may be due to fitting magnitude images that are contaminated with noise in the late echoes. The discrepancy is removed, if the curve fitting is applied to the images obtained by nonlinear inversion as described in (13).

DISCUSSION

Model-based reconstructions of parametric maps serve several purposes: they may contribute to a reduction of the measuring time or—for a constant measuring time—improve the image quality (e.g., by increasing the spatial resolution) and/or enhance the scanning efficiency (e.g., by allowing for more sections). Most importantly, however, their main advantage is the access to quantitative (objective and comparable) measures of tissue properties. For the clinically relevant case of T2 relaxation, the present work offers a relatively simple solution that uses a standard spin-echo MRI sequence with multiple echoes and Cartesian encoding. It requires only a minor modification for implementing the desired undersampling scheme. The calculation of differently T2-weighted images (from fully sampled *k*-space data) is no longer necessary and the retrospective fitting by a T2 relaxation decay is replaced by a direct nonlinear inverse reconstruction of a spin-density and T2 map.

In general, the success of a model-based reconstruction depends on the ability to accurately model the underlying data dependency. In this study, the chosen model forces the optimizer to "explain" the signal behavior by a mono-exponential decay. Image regions or pixels which do not comply with this assumption (e.g., tissues with a multi-exponential signal decay or structural borders with pronounced T2 discontinuities) may, therefore, lead to artifacts in the reconstruction. While an appropriate undersampling scheme could be shown to avoid the problem, it is also possible to extend the reconstruction by a less restrictive model function such as a multi-exponential decay.

It is conceivable to further improve the reconstruction by incorporating prior knowledge into the cost function using suitable regularization terms. For example, penalizing the total variation of the maps may suppress ringing artifacts and preclude noise amplifications during the iterative optimization. However, because there is no generally accepted method for objectively choosing the inherent regularization parameters, we left this option for future extensions. We also found that in most cases a much lower number of iterations turned out to be sufficient for accurate reconstruction. Therefore, an automatic stopping criterion for the optimization would be highly desirable. Finally, for more widespread practical applications, we expect a substantial reduction of the computational

Table 2
T2 Relaxation Times From Model-Based Reconstructions of the Human Brain

		Undersampling factor			
	Standard fitting	1	2	5	10
Anterior cingulate	100 ± 10	99 ± 10	98 ± 10	98 ± 10	98 ± 10
Insular cortex	94 ± 5	93 ± 5	93 ± 5	92 ± 5	93 ± 6
Thalamus	81 ± 4	79 ± 4	78 ± 4	78 ± 5	78 ± 8
Lentiform nucleus	78 ± 4	77 ± 8	77 ± 5	76 ± 5	78 ± 6
Caudate nucleus	88 ± 5	87 ± 5	86 ± 5	86 ± 5	87 ± 9
Internal capsule	56 ± 5	54 ± 6	55 ± 6	52 ± 7	54 ± 12
Frontal white matter	74 ± 2	74 ± 2	73 ± 2	72 ± 2	74 ± 4

*T2 values (ms) represent mean ± SD (16 echoes, ΔTE = 12.2 ms, 32-element coil). Standard nonlinear least-squares fitting refers to a set of fully sampled T2-weighted magnitude images.

time with the use of graphical processing units as most of the calculations may be performed in parallel.

In conclusion, depending on the available SNR, the proposed method allows for very high undersampling factors by exploiting data redundancy in parameter space, even without the need for data redundancy due to multiple receiver coils. Thus, the method effectively works without parallel imaging in settings where only a single or very few coils are available. This feature is of particular interest for animal MRI studies, where coil arrays with more than four elements are far less common than in state-of-the-art human MRI systems. On the other hand, the availability of multiple receiver coils not only ensures optimum SNR, but further improves the quality of the undersampled reconstructions. Accordingly, the combined data redundancies from multiple coils and multiple echoes provide access to the largest undersampling factors that clearly exceed the values commonly obtained by conventional parallel MRI. It should also be emphasized that the automatic gradient-scaling method developed here removes the need for manually tuning the algorithm for different anatomical regions or MRI systems.

REFERENCES

1. Hennig J, Nauerth A, Friedburg H. RARE imaging: a fast imaging method for clinical MR. Magn Reson Med 1986;3:823–833.
2. Pruessmann KP, Weiger M, Scheidegger MB, Boesiger P. SENSE: sensitivity encoding for fast MRI. Magn Reson Med 1999;42: 952–962.
3. Sodickson DK, Manning WJ. Simultaneous acquisition of spatial harmonics (SMASH): fast imaging with radiofrequency coil arrays. Magn Reson Med 1997;38:591–603.
4. Lustig M, Donoho D, Pauly JM. Sparse MRI: the application of compressed sensing for rapid MR imaging. Magn Reson Med 2007;58:1182–1195.
5. Doneva M, Börnert P, Eggers H, Stehning C, Senegas J, Mertins A. Compressed sensing reconstruction for magnetic resonance parameter mapping. Magn Reson Med 2010;64:1114–1120.
6. Graff C, Li Z, Bilgin A, Altbach M, Gmitro AF, Clarkson EW. Iterative T2 estimation from highly undersampled radial fast spin-echo data. Proc Intl Soc Mag Reson Med 2006;14:925.
7. Block KT, Uecker M, Frahm J. Model-based iterative reconstruction for radial fast spin-echo MRI. IEEE Trans Med Imaging 2009;28:1759–1769.
8. Olafsson VT, Noll DC, Fessler JA. Fast joint reconstruction of dynamic R2* and field maps in functional MRI. IEEE Trans Med Imaging 2008;27:1177–1188.
9. Uecker M, Hohage T, Block KT, Frahm J. Image reconstruction by regularized nonlinear inversion - joint estimation of coil sensitivities and image content. Magn Reson Med 2008;60:674–682.
10. Gibbs JW. Fourier's series. Nature 1898;59:200.
11. Gibbs JW. Fourier's series. Nature 1899;59:606.
12. Bôcher M. Introduction to the Theory of Fourier's Series. Ann Math 1906;7:81–152.
13. Wilbraham H. On a certain periodic function. Cambridge Dublin Math 1848;3:198.
14. Hager WW, Zhang H. A new conjugate gradient method with guaranteed descent and an efficient line search. SIAM J Optim 2006;16:170–192.